JOURNAL OF GEOPHYSICAL RESEARCH, VOL. 104, NO. D3, PAGES 3773–3788, FEBRUARY 20, 1999

# Mesospheric Na layer at 40°N: Modeling and observations

John M. C. Plane,[1] Chester S. Gardner,[2] Jirong Yu,[3] C. Y. She,[4]
Rolando R. Garcia,[5] and Hugh C. Pumphrey[6]

**Abstract.** A complete monthly record of the annual variation of Na and temperature in the upper mesosphere has been obtained from 3 years of nighttime lidar observations at two midlatitude sites, Urbana-Champaign, Illinois (40° N), and Fort Collins, Colorado (41° N). The Na density exhibits a strong annual variation at all heights between 81 and 107 km, with the column abundance of the layer peaking in early winter and then decreasing by nearly a factor of 4 to a midsummer minimum. There are also significant semiannual components to the variations in the centroid height and thickness of the layer. The nighttime temperature profile between 81 and 105 km exhibits a high winter mesopause at about 101 km and a summer mesopause at about 85 km. During spring and autumn, the mesopause oscillates apparently randomly between these states. A seasonal model of the Na layer was then constructed incorporating recent laboratory studies of the pertinent neutral and ionic reactions of the metal. The background atmospheric composition was provided from three off-line models, as well as from UARS/Microwave Limb Sounder satellite measurements of $H_2O$. With a small number of permitted adjustable parameters, the model is able to reproduce many observed features of the Na layer remarkably well, including the monthly variation in column abundance and layer shape. The biggest discrepancy is during midsummer, when the modeled layer is displaced 2-3 km above that observed, although a factor contributing to this is that the lidar observing period during summer was relatively short and the effect of the diurnal tide could have been incompletely sampled. Both the observations and the model show that Na density and temperature are highly correlated below 96 km (correlation coefficient equal to 0.8-0.95), mostly as a result of the influence of odd oxygen/hydrogen chemistry on the partitioning of sodium between atomic Na and its principal reservoir species, $NaHCO_3$. Above 96 km, a weak negative correlation (-0.2) is explained by the dominance of ion-molecule chemistry. Finally, it was shown that if the eddy diffusion coefficient in the middle mesosphere is significantly smaller or if the global meteoric influx is much larger than the values used in the present model, then processes for permanently removing gas-phase Na species in the mesosphere, such as polymerisation and deposition onto dust particles, will need to be included.

## 1. Introduction

Meteoric ablation is the major source of a layer of atomic Na that occurs globally in the upper mesosphere [*Plane*, 1991]. Lidar observations of this layer were first made in England soon after the invention of the tuneable dye laser [*Bowman et al.*, 1969], and since then numerous ground-based and airborne observations have been reported from locations as far north as Franz Joseph Land to as far south as the South Pole [e.g., *Juramy et al.*, 1981; *Collins et al.*, 1994]. Advances in laser technology led to the first measurements, by observing the hyperfine structure of the atomic Na *D*-lines, of mesospheric temperatures in 1979 [*Gibson et al.*, 1979] and winds in 1991 [*Bills et al.*, 1991b]. In 1989, our groups at Colorado State University and the University of Illinois jointly developed a new two-frequency Na temperature lidar technique based on a narrowband CW oscillator/pulsed dye amplifier laser system [*She et al.*, 1990; *Bills et al.*, 1991a]. Routine observations have been made at Fort Collins, Colorado (41° N), and Urbana-Champaign, Illinois (40° N), since 1991 using this new technique. The data collected at both sites from 1991 through mid-1994 have been combined here to study the seasonal variations of the nighttime Na layer and mesopause region temperature structure.

This data set presents a rare opportunity to test the current generation of models that have been developed to understand the appearance and characteristics of the Na layer [e.g., *Helmer and Plane*, 1993; *McNeil et al.*, 1995; *Plane et al.*, 1998]. Historically, there have been two related difficulties in model development. The first is that although the Na layer itself can be observed with exquisite time and height resolution by modern lidars, and $Na^+$ ions can be measured (albeit infrequently) by rocket-borne mass spectrometry, the molecular sodium species that must exist in the atmosphere cannot currently be observed. Instead, an understanding of the chemistry that controls the Na

[1]School of Environmental Sciences, University of East Anglia, Norwich, England, U.K.
[2]Department of Electrical and Computer Engineering, University of Illinois at Urbana-Champaign.
[3]NASA Langley Research Center, Hampton, Virginia.
[4]Department of Physics, Colorado State University, Fort Collins.
[5]National Center for Atmospheric Research, Boulder, Colorado.
[6]Department of Meteorology, University of Edinburgh, Edinburgh, Scotland, U.K.



Paper number 1998JD100015.
0148-0227/99/1998JD100015$09.00

layer has necessarily been based on laboratory studies of the pertinent chemical reaction kinetics [*Plane*, 1991]. However, the second difficulty has been that studies of the reaction kinetics of neutral sodium species at low temperatures are technically challenging, and it was not until the mid-1980s that such laboratory data started to become available. Since then, much has been learned about the gas-phase chemistry of sodium and other meteoric metals (for a review, see *Plane and Helmer* [1994]).

Figure 1 is a schematic drawing which illustrates the chemical reactions connecting the major Na species that are believed to exist in the upper mesosphere [*Plane et al.*, 1998]. Below the peak of the Na layer at about 90 km, Na is converted to its major reservoir species, $NaHCO_3$, by a sequence of reactions involving principally $O_3$, $H_2O$, and $CO_2$. We have shown using theoretical quantum calculations [*Rajasekhar and Plane*, 1993] that the bicarbonate is very stable thermodynamically: its only likely reaction is conversion back to atomic Na by reaction with H (reaction (17) in Table 1). Indeed, in experiments currently underway at the University of East Anglia, we have confirmed that this reaction occurs very slowly, as required by atmospheric models [*Helmer and Plane*, 1993].

The importance of the reaction between $NaHCO_3$ and H is that it should control the lifetime of $NaHCO_3$ and hence the removal of atomic Na on the underside of the layer, where the very small scale height (<3 km) provides a challenging test for models. Other removal mechanisms that have been proposed previously include the deposition of Na and its compounds onto dust particles [*Hunten*, 1981], and the formation of hydrated cluster ions [*Jegou et al.*, 1985]. However, unlike the gas-phase chemistry illustrated in Figure 1, nearly all of which has now been studied in the laboratory, there is little evidence for either of these other mechanisms playing a major role in the mesosphere below 90 km. A further challenge for models is to account for the small scale height on the top side of the layer, above 90 km. In this region, the major sodium reservoir is $Na^+$, which is coupled to Na by the ion-molecule chemistry shown in Figure 1. Recent laboratory studies [*Cox and Plane*, 1997, 1998; *Levandier et al.*, 1997] have now placed most of this chemistry on a secure footing.

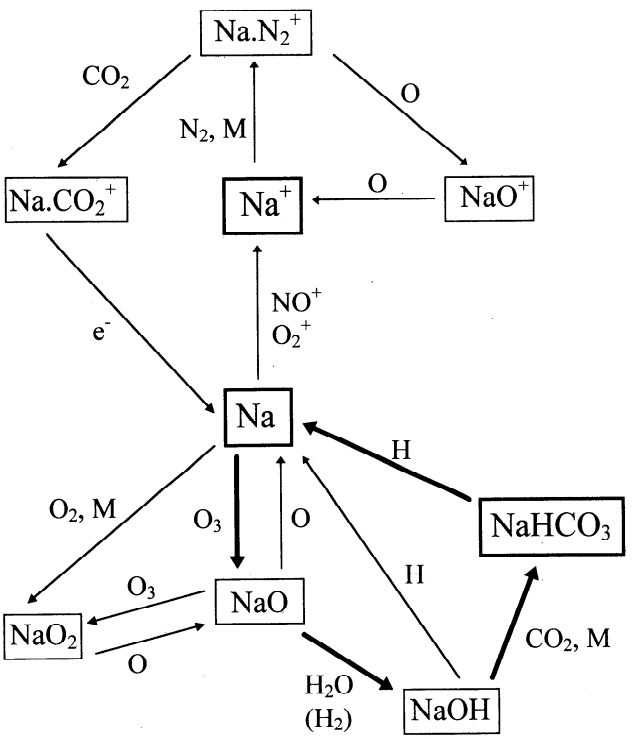


**Figure 1.** Schematic drawing of the important cycles of sodium in the upper mesosphere ($NaO_3$ and $NaCO_3$ are not included for the sake of clarity). The major sodium species are in the thick-edged boxes, and the cycle coupling Na to $NaHCO_3$ is shown with bold arrows.

When evaluating the predictions of a sodium model against a set of lidar observations, there are several potential difficulties. First, the input of sodium from meteor ablation is sporadic, both temporally and spatially. Second, the concentration profiles of the species such as $O_3$, $H_2O$, O, H, $NO^+$, and electrons, that control the rates of the reactions in Figure 1, are usually not measured contemporaneously with the lidar observations. Even in a combined lidar and rocket experiment of the kind described by *Clemesha et al.* [1995], the derivation of the concentrations of some of these minor species from rocket-borne airglow measurements is indirect. Third, the vertical profiles of all of these minor species are subject to rapid perturbations by gravity waves, tides, and winds. One way to overcome these problems is to average the lidar data to produce daily, monthly, or even seasonal average profiles. Estimates of the concentration profiles of the controlling minor species can then be obtained from zonally averaged models and satellite data. This is the approach that we have adopted for the present study.

The sodium model that we will employ was originally developed by *Plane* [1991] and then optimized by *Helmer and Plane* [1993] to a wintertime profile at high latitude (69° N) [*Tilgner and von Zahn*, 1988]. This model has since been applied successfully to summertime profiles at the South Pole and in the Canadian Arctic (62°-68° N) [*Plane et al.*, 1998], and to an autumn profile at Haleakala, Hawaii (20° N) [*Swenson et al.*, 1998]. *McNeil et al.* [1995] have also used a similar model to account for the observed positive correlation between Na layer abundance and temperature reported at midlatitudes by *Kane and Gardner* [1993]. Notwithstanding this recent progress, the very extensive data set collected in the present study permits, for the first time, a detailed test of a sodium model over a complete annual cycle.

## 2. Na Lidar Observations

The narrowband Na temperature lidar technique is described in considerable detail in several earlier publications [*Bills et al.*, 1991a; *She et al.*, 1992; *Papen et al.*, 1995]. Measurements are obtained by tuning the laser successively to $f_a$, the peak of the Na $D_{2a}$ fluorescence line, and to the crossover frequency $f_c$, midway between the $D_{2a}$ and $D_{2b}$ lines [see *Bills et al.*, 1991a, Figure 1]. The ratio ($R_T$) of the received Na signal at $f_c$ to the signal at $f_a$ is a sensitive function of temperature ($T$). The relationships between $R_T$ and $T$, and between the sum of the $f_a$ and $f_c$ signals and Na density, are determined using detailed quantum mechanical models of the Na $D_2$ absorption and fluorescence spectra [*She et al.*, 1992; *Papen et al.*, 1995]. The temperature and Na density profiles are computed iteratively: because the Na cross sections at $f_a$ and $f_c$ depend upon $T$, the temperature profile is used to compute the Na density profile; likewise, because extinction of the upwardly propagating laser beam and the downwardly propagating fluorescence signal within the Na layer

**Table 1.** Neutral and Ionic Gas-Phase Reactions of Na Species in the Upper Mesosphere

| Reaction No. | Reaction | Rate Coefficient[a] | Source |
|---|---|---|---|
| | *Neutral Chemistry With Oxygen Only* | | |
| (R1) | $Na + O_3 \rightarrow NaO + O_2$ | $1.1 \times 10^{-9} \exp(-116/T)$ | 1 |
| (R2) | $NaO + O \rightarrow Na + O_2$ | $2.2 \times 10^{-10} (T/200)^{1/2}$ | 1 |
| (R3) | $Na + O_2 + M \rightarrow NaO_2 + M$ | $5.0 \times 10^{-30} (T/200)^{-1.22}$ | 1 |
| (R4a) | $NaO + O_3 \rightarrow NaO_2 + O_2$ | $1.1 \times 10^{-9} (\exp(-568/T)$ | 1 |
| (R4b) | $NaO + O_3 \rightarrow Na + 2O_2$ | $3.2 \times 10^{-10} (\exp(-550/T)$ | 1 |
| (R5) | $NaO + O_2 + M \rightarrow NaO_3 + M$ | $5.3 \times 10^{-30} (T/200)^{-1}$ | 1 |
| (R6) | $NaO_2 + O \rightarrow NaO + O_2$ | $5.0 \times 10^{-10} \exp(-940/T)$ | 1 |
| (R7) | $NaO_3 + O \rightarrow Na + 2O_2$ | $2.5 \times 10^{-10} (T/200)^{1/2}$ | 2 |
| | *Neutral Chemistry With H, O, $H_2$, $H_2O$ and $CO_2$* | | |
| (R8) | $NaO + H_2O \rightarrow NaOH + OH$ | $4.4 \times 10^{-10} \exp(-507/T)$ | 3 |
| (R9a) | $NaO + H_2 \rightarrow NaOH + H$ | $1.1 \times 10^{-9} \exp(-1100/T)$ | 1 |
| (R9b) | $NaO + H_2 \rightarrow Na + H_2O$ | $1.1 \times 10^{-9} \exp(-1400//)$ | 1 |
| (R10) | $NaO + H \rightarrow Na + OH$ | $3.0 \times 10^{-10} \exp(-668/T)$ | 1 |
| (R11) | $NaO_2 + H \rightarrow Na + HO_2$ | $1 \times 10^{-9} \exp(-1000/T)$ | 2 |
| (R12) | $NaOH + H \rightarrow Na + H_2O$ | $4 \times 10^{-11} \exp(-550/T)$ | 2 |
| (R13) | $NaO + CO_2 + M \rightarrow NaCO_3 + M$ | $1.3 \times 10^{-27} (T/200)^{-1}$ | 1 |
| (R14) | $NaCO_3 + O \rightarrow NaO_2 + CO_2$ | $5 \times 10^{-10} \exp(-1200/T)$ | 2 |
| (R15) | $NaCO_3 + H \rightarrow NaOH + CO_2$ | $1 \times 10^{-9} \exp(-1400/T)$ | 1 |
| (R16) | $NaOH + CO_2 + M \rightarrow NaHCO_3 + M$ | $1.9 \times 10^{-28} (T/200)^{-1}$ | 1 |
| (R17) | $NaHCO_3 + H \rightarrow Na + H_2O + CO_2$ | $1 \times 10^{-12} \exp(-590/T)$ | 6 |
| | *Ion-molecule Chemistry* | | |
| (R18) | $Na + O_2^+ \rightarrow Na^+ + O_2$ | $2.7 \times 10^{-9}$ | 4 |
| (R19) | $Na + NO^+ \rightarrow Na^+ + NO$ | $8.0 \times 10^{-10}$ | 4 |
| (R20) | $Na^+ + N_2 + M \rightarrow Na.N_2^+ + M$ | $4.8 \times 10^{-30} (T/200)^{-2.2}$ | 5 |
| (R21) | $Na.N^{2+} + X \rightarrow Na.X^+ + N_2$ (X = $CO_2$, $H_2O$) | $8 \times 10^{-10}$ | 5 |
| (R22) | $Na.N_2^+ + O \rightarrow NaO^+ + N_2$ | $6 \times 10^{-10}$ | 5 |
| (R23) | $NaO^+ + O \rightarrow Na^+ + O_2$ | $8 \times 10^{-10}$ | 5 |
| (R24) | $Na.Y^+ + e^- \rightarrow Na + Y$ (Y = $N_2$, $CO_2$, $H_2O$, O) | $1 \times 10^{-6} (T/200)^{1/2}$ | 2 |
| | *Photochemical Reactions* | | |
| (R25) | $NaO_2 + h\upsilon \rightarrow Na + O_2$ | $4 \times 10^{-3}$ | 1 |
| (R26) | $NaOH + h\upsilon \rightarrow Na + OH$ | $1 \times 10^{-3}$ | 2 |
| (R27) | $NaO_3 + h\upsilon \rightarrow NaO + O_2$ | $1 \times 10^{-4}$ | 2 |
| (R28) | $Na + h\upsilon \rightarrow Na^+ + e^-$ | $2 \times 10^{-5}$ | 1 |

References: 1, measured by various workers [see *Plane and Helmer*, 1994]; 2, estimated [*Helmer and Plane*, 1993]; 3, *Cox and Plane* [1998b]; 4, measured [*Levandier et al.*, 1997]; 5, measured/calculated [*Cox and Plane*, 1998a]; 6, fitted (see text).

[a]Rate coefficient units: unimolecular, $s^{-1}$; bimolecular, $cm^3$ $molecule^{-1}$ $s^{-1}$; termolecular, $cm^6$ $molecule^{-2}$ $s^{-1}$

depends on Na density and is different at $f_a$ and $f_c$, the density profile is then used to compute the temperature profile.

We report data collected from January 1991 until April 1994 on 147 nights at Fort Collins, Colorado, and 75 nights at Urbana-Champaign, Illinois. Observations were conducted at night, typically from dusk until dawn when weather permitted. The observation periods varied from 2 hours to almost 10 hours with a mean of approximately 6 hours, with weather being the most significant factor limiting observations at both sites. Data gaps as large as a month or more in the annual data sets at both sites constrain the usefulness of either data set for studying the seasonal variability of the Na layer and temperature structure. However, by combining all the data acquired at both sites between 1991 and April 1994, the longest data gap is only 4 days. The combined data sets include approximately 1285 hours of observations on 222 nights distributed approximately uniformly throughout the year. This corresponds to a monthly average of 99 hours of observations, spread over 17 observation periods. The hours of observation were generally smaller during summer months because of the shorter nights: the average observation period was 4.7 hours in midsummer, compared with 7.9 hours in midwinter.

The dominant sources of error in the individual profiles of Na density and temperature are photon noise, laser frequency errors, and Na density fluctuations during data acquisition. *Papen et al.* [1995] have discussed these error sources in detail and provided estimates of their magnitudes for the Illinois data. Because the Colorado and Illinois lidars are similar in design and both groups employ the same processing procedures to generate the temperature and Na density profiles, the errors in both data sets are comparable. The temporal resolution of the profiles is nominally 5 min, with height resolutions of 1 km for temperature and 48 m for Na density. The accuracy of the temperature profiles depends primarily on signal level and is typically ± 3 K at the Na layer peak near 92 km, where the signal is strongest, and ± 10 K at the top and bottom edges of the layer near 102 and 84 km, where the signal is weakest. For this study, the temperature and Na density profiles were averaged over the

whole observation period for each night (average 6 hours) and then smoothed vertically using a Hamming window with a full width of 2 km. The absolute accuracy of the nightly mean temperature profiles is estimated to be ±2 K throughout the complete altitude range. The absolute accuracy of the nightly mean Na density profiles is limited to ±10% by the accuracies of the assumed calibration constants.

Gravity waves, planetary waves, and tides can have substantial influences on the structure of the Na layer and are largely responsible for the observed night-to-night variability. Although averaging over the whole night does reduce fluctuations caused by gravity waves, the inertial period at 40° N (18.7 hours) is much larger than the mean observation period (6 hours) so that substantial gravity wave effects remain (vide infra). Because an important objective of this study is to compare the observed Na layer with an atmospheric model which does not explicitly include the pseudorandom effects of waves and tides, the nightly mean Na profiles were further smoothed to reduce or eliminate residual wave effects. This was done using a Hamming window with a full width of 45 days, which is roughly equivalent to using a rectangular window with a full width of 3 weeks. The nightly temperature profiles were smoothed seasonally in the same manner. Even so, recent 24 hour observations of Na and temperature have shown that the diurnal tide can exceed 15 K at mesopause heights, larger than existing model predictions [*Yu et al.*, 1997; *States and Gardner*, 1998]. When observations are restricted to nighttime, such as those reported here, incomplete sampling of the diurnal tide can lead to temperature biases of several K.

## 3. Description of the Sodium Model

The development of the sodium model that was used for this study has been described previously [*Plane*, 1991; *Helmer and Plane*, 1993; *Plane et al.*, 1998], and so here we will focus on its extension to a seasonal model with a 1-month time resolution. The original one-dimensional model, which extends from 65 to 110 km, assumes that meteor ablation is the major source of sodium in the upper atmosphere. A second and key assumption is that gas-phase chemistry essentially controls the formation of the layer of atomic Na centered at about 90 km, and that the chemistry is closed: that is, all the constituent species (Na, $Na^+$, Na cluster ions, NaO, $NaO_2$, $NaO_3$, NaOH, $NaCO_3$, and $NaHCO_3$) cycle between each other (Figure 1), so that none of these species provides a permanent sink removing sodium from the system.

The continuity equation for the $i$th species with concentration $n_i$ is given by

$$\frac{dn_i}{dt} - P_i + L_i - I_i + \nabla\Phi_i = 0 \qquad (1)$$

where $P_i$ and $L_i$ are the chemical production and loss terms, respectively, $I_i$ is the injection rate from meteoric ablation, and $\Phi_i$ is the vertical flux of $i$. Summing over all sodium-containing species $i$ and applying the law of mass action to $P_i$ and $L_i$, we obtain

$$\frac{dn(\mathrm{Na})}{dt} = \sum_i (I_i - \nabla\Phi_i) = I(\mathrm{Na}) - \nabla\Phi(\mathrm{Na}) \qquad (2)$$

where $n$(Na) is the total sodium concentration, $I$(Na) is the total injection rate, and $\Phi$(Na) is the total flux of all sodium species. Under time-averaged conditions, both sides of equation (2) should be zero.

A further key assumption is that the rate of partitioning of sodium among its constituent species is rapid on the timescale of vertical mixing. Hence a local chemical steady state operates at each level (or altitude) in the model. The validity of this last assumption was demonstrated recently by *Plane et al.* [1998]. Since the transport of all the sodium constituents is governed by the same eddy diffusion coefficient up to the turbopause at about 105 km, the vertical flux of total sodium at height $z$ is then given by

$$\Phi(\mathrm{Na}) = -K_E\left[\frac{dn(\mathrm{Na})}{dz} + n(\mathrm{Na})\left(\frac{1}{H} + \frac{1}{T}\frac{dT}{dz}\right)\right] \qquad (3)$$

where $K_E$ is the eddy diffusion coefficient, $H$ is the atmospheric scale height, and $T$ the temperature [*Thomas*, 1974]. Note that $\Phi$(Na) is equal to the integrated ablation of sodium from $z$ upward, under time-averaged conditions. Hence equation (3) can be solved for $n$(Na) as a function of $z$.

In the present study, the inputs required for the solution were as follows. First, the meteoric ablation flux of total sodium (i.e., Na, $Na^+$, and other chemically labile species such as NaO and $Na_2O$) was set to an annual mean of $\Phi$(Na) = 1.3 ¥ $10^4$ $cm^{-2}$ $s^{-1}$ [*Plane*, 1991], with the monthly variation in meteoric flux scaled to the observational data of *Hughes* [1978]. Second, the meteoric ablation profile of *Hunten et al.* [1980] was used. This was derived assuming a mean meteoric infall velocity of 15 km $s^{-1}$, which produces a peak ablation height of 83 km. Although there is now evidence from meteor radar work for a small population of faster moving particles that ablate higher up [*Elford et al.*, 1995], the solution of the continuity equation is only weakly dependent on the precise choice of ablation profile. Third, the monthly profiles of temperature and pressure at 40° N were taken from the Na lidar data in this study and *Committee on Space Programs and Research (COSPAR)* [1990], respectively. The average profile of the eddy diffusion coefficient was taken as the summertime profile from *Danilov and Kalgin* [1992], which ranges from 3.5 x $10^5$ $cm^2$ $s^{-1}$ at 65 km to 1.4 x $10^6$ $cm^2$ $s^{-1}$ at 95 km, and is in excellent agreement above 80 km with the review by *Hocking* [1990]. Above 100 km, a molecular diffusion term was added. The monthly eddy diffusion coefficient profiles were then obtained by scaling this profile according to the monthly variations from the two-dimensional model of *Garcia and Solomon* [1994] (hereafter designated the G-S model). This choice of $K_E$ is discussed further in the section on model sensitivity. The atmospheric density above 80 km was calculated by taking the *COSPAR* [1990] monthly pressure at 80 km and solving the hydrostatic equation with the lidar temperature profile up to 105 km. Finally, the solution of the continuity equation requires the total sodium to be specified at a reference altitude. Recent models of the Na layer [e.g., *McNeil et al.*, 1995; *Plane et al.*, 1998] indicate that more than 90% of the total sodium at 95 km is in the form of atomic Na, and so we have usually adopted this as the reference altitude because the total sodium could then be inferred from lidar observations. However, in the present study where we are attempting to explain the seasonal differences in the Na layer, this procedure would systematically bias the model toward producing good agreement with the observations. Hence we have used the bottom level of the model at 65 km as the reference altitude. The mean total sodium at 65 km was therefore designated as a single adjustable parameter, scaled on a monthly basis by the relative meteoric input flux of *Hughes* [1978].

Solution of the continuity equation yields the vertical profile of total sodium. The concentrations of the constituent Na species at each altitude are then computed by assuming a chemical steady state governed by the set of reactions listed in Table 1. Note that the ion-molecule rate coefficients $k_{18}$-$k_{23}$ have changed slightly from a previous version of the model [*Plane et al.*, 1998] following very recent laboratory measurements [*Levandier et al.*, 1997; *Cox and Plane*, 1997, 1998]. The Arrhenius parameters characterizing the rate coefficient for reaction (17) are treated in the model as adjustable parameters, with the constraint that $k_{17}$ extrapolates to the same values that were employed in our recent study of the Na layer at high latitudes in summer [*Plane et al.*, 1998], when the mesopause temperature is considerably colder.

Application of the steady state also requires the monthly concentration profiles of the minor species which control the sodium chemistry (Figure 1). Initially, the vertical profiles of $O_3$, O, H, $H_2$, $H_2O$, and $CO_2$ for midnight at 38°N were taken from the G-S model. Because the monthly average temperatures measured by the Na lidars during the course of this study were somewhat warmer than the zonally averaged monthly temperature profiles in the G-S model (vide infra), the $O_3$ concentration was recalculated from the concentrations of O and H in the G-S model, by assuming a steady state was established between production and loss by the reactions

(R29) $O + O_2 + M \rightarrow O_3 + M$ $\quad k_{29} = 5.6 \times 10^{-34} (T/298)^{-2.8}$ cm$^6$ molecule$^{-2}$ s$^{-1}$

(R30) $H + O_3 \rightarrow OH + O_2$ $\quad k_{30.} = 1.4 \times 10^{-10} \exp(-470/T)$ cm$^3$ molecule$^{-1}$ s$^{-1}$

where the rate coefficients are taken from *DeMore et al.* [1994]. The concentration of atomic H is much less temperature-dependent because the OH formed in reaction (30) (and $HO_2$ formed by recombination between H and $O_2$) are cycled back to H by fast reactions with atomic O which have only slight negative temperature dependences. The monthly profiles of $NO^+$, $O_2^+$, and $e^-$ were taken from the International Reference Ionosphere 1995 model for midnight at 40°N [*Bilitza et al.*, 1993].

Atomic O plays a pivotal role in the balance between Na and its reservoir, $NaHCO_3$, both directly through reactions (2) and (6) (see Table 1 and Figure 1), and indirectly through reactions (12) and (17) which involve atomic H. We therefore also ran the present Na model using atomic O and H profiles from the semiempirical model MSIS-E-90 [*Hedin*, 1991], recalculating the $O_3$ profiles by assuming steady state as described above. $H_2O$ is another atmospheric species that is central in controlling the conversion of Na to $NaHCO_3$ through reaction (8). Recently, *Pumphrey and Harwood* [1997] have reported global measurements of upper mesospheric $H_2O$ using the Microwave Limb Sounder on the UARS platform. A prototype retrieval of the zonally averaged water vapor mixing ratio is now available, and the individual measurements are believed to be useful at altitudes below 85 km. Above this altitude, they revert rapidly to a reasonably intelligent guess. Nevertheless, the resulting monthly profiles at 40°N provide a good test of the dynamical mixing of mesospheric $H_2O$ that is contained in the zonally averaged G-S model. Figure 2 illustrates a comparison between the annual variation of $H_2O$ between 65 and 94 km measured by UARS and that predicted by G-S with the Prandtl number (the ratio of the eddy diffusion coefficient to the momentum diffusion coefficient) set to $Pr$ = 5. This demonstrates very satisfactory agreement, both in the absolute concentrations and the seasonal variation of $H_2O$. Not surprisingly, use of $H_2O$ profiles from either the G-S model or the UARS measurements produced essentially the same outcome in the modeling runs described below. It may be noted that a value of $Pr$ = 5, rather than close to 1, has been recommended in a recent detailed study by *Thomas* [1996, and references therein].

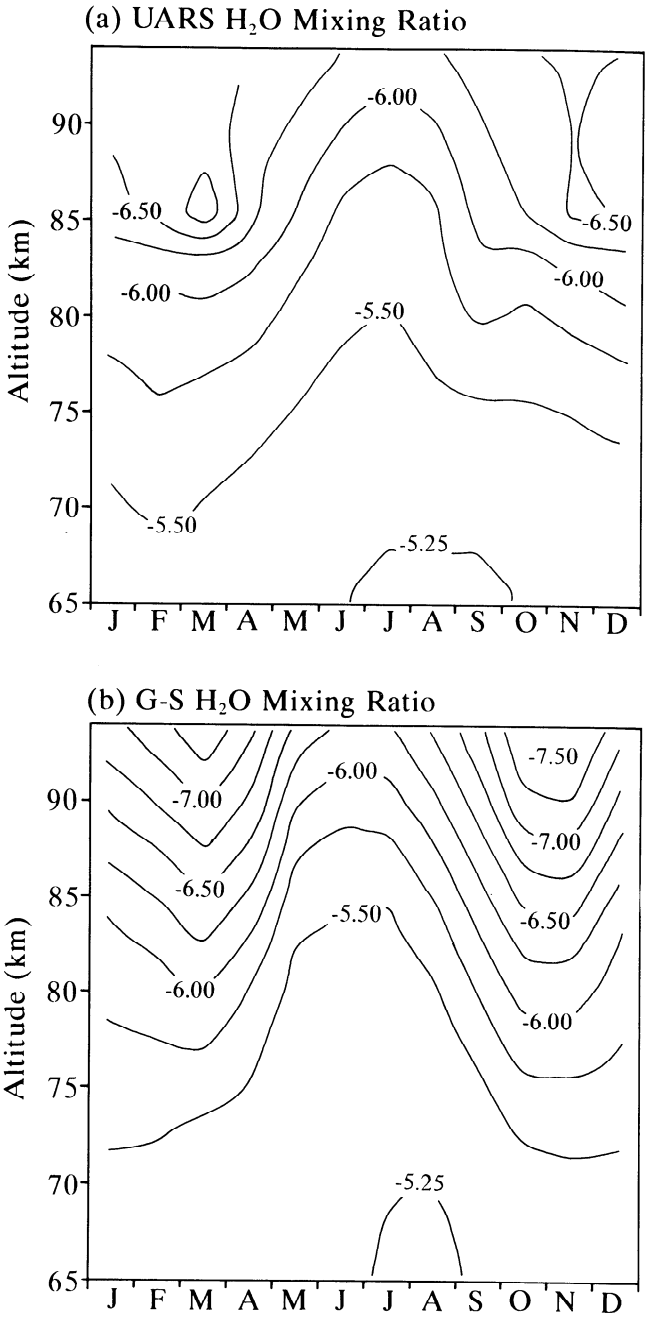


**Figure 2.** Contour plots of the zonally averaged $H_2O$ mixing ratio at 40°N, versus altitude and time: (a) measured by the Microwave Limb Sounder on the UARS platform, over a period of 600 days between 1991 and 1993; (b) predicted by the Garcia-Solomon model with a Prandtl number of 5.

## 4. Modeling the Observations

In order to provide a strict test of the model's ability to predict the seasonal variation in the Na layer, we allowed only three of the unknown parameters in the model to be adjustable

when optimizing to the observations. These parameters were the annual mean total sodium concentration at 65 km required for integrating the continuity equation (vide supra), which was set to $2.2 \times 10^5$ cm$^{-3}$; and the two Arrhenius parameters of $k_{17}$ (listed in Table 1). These three parameters were optimized to reproduce the observed column abundance, centroid height, and root-mean-square (rms) width of the annual mean Na layer. The other unmeasured rate coefficients in Table 1 were left unchanged from an earlier version of the model applied to a wintertime Na profile from a northern high-latitude station (Andoya, 69°N) [*Helmer and Plane*, 1993], apart from minor modifications to incorporate the results of recent laboratory kinetic studies [*Plane et al.*, 1998].

When the Na model was run with the profiles of atomic O from the G-S model, the scale height on the underside of the layer below 90 km was found to be systematically smaller (by 0.5 to 1 km) than that observed. By contrast, the MSIS-E-90 model predicts a less steep falloff in atomic O below 90 km, and hence produced better agreement with the Na lidar measurements. The falloff in atomic O is largely a balance between downward transport from above 90 km and removal by recombination with $O_2$. Hence, because the atomic O concentration decreases by several orders of magnitude in a few kilometres, the predicted falloff as a function of height is extremely sensitive to the model parameterization of vertical transport. Since the aim of the present study was to construct and test a seasonal sodium model with the most appropriate ancillary data on atmospheric composition, we therefore adopted the MSIS-E-90 profiles of O and H for the modeling runs described below, while recognizing that this entailed a sacrifice in self-consistency.

Figure 3 compares the modeled and observed Na profiles at 40°N for September. As expected, $Na^+$ and $NaHCO_3$ are the major sinks for the metal on the top and bottom sides of the layer, respectively. The MSIS-E-90 profile of atomic O is also shown in Figure 3 to emphasize the importance of the falloff in the atomic O concentration between 80 and 90 km in controlling the underside of the Na layer. In the future, it may be possible to exploit this relationship in order to measure the falloff in atomic O through lidar observations of Na, and also to optimize parameterizations of transport such as the Prandtl number in models.

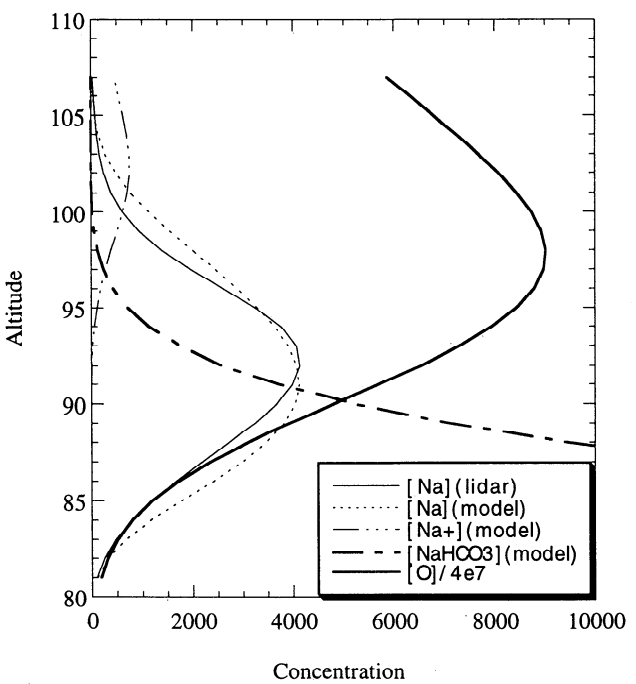


**Figure 3.** Measured and modeled profiles of the atomic Na density at 40°N during September. Also shown are the modeled profiles of the other major sodium species, $Na^+$ and $NaHCO_3$, and the atomic O profile from the MSIS-E-90 model (reduced by a factor of $4 \times 10^7$).

## 5. Results and Discussion

### 5.1. Seasonal Variations in Na Density

Figure 4 illustrates the observed profiles of atomic Na (plotted on a logarithmic concentration scale) for each month. Over the altitude ranges where the Na density exceeds 200 cm$^{-3}$, the smoothed profiles are well approximated by Gaussian distributions of the form

$$[\mathrm{Na}]_z = \frac{A_S}{\sqrt{2\pi}\sigma_S} \exp\left[\frac{-(z-z_O)^2}{2{\sigma_S}^2}\right] \quad (4)$$

where $A_S$ is the column abundance, $z_0$ is the centroid height, and $\sigma_S$ is the rms width. These parameters for each monthly profile are tabulated in Table 2. Also shown in the panels in Figure 4 is the modeled Na profile. For the months of January through April, and September through December, there is excellent agreement with the observed peak height and density, and the top and bottom scale heights of the layer. By contrast, in the summer months, especially June and July, the modeled layer is displaced about 2-3 km above that observed, although the peak density and layer shape, and hence the column abundance, are still in good agreement.

Plates 1a and 1b are contour plots showing the observed and modeled Na density as a function of altitude and month. Overall, the model reproduces the layer morphology and the absolute concentration changes in the layer between the summer minimum and early winter maximum very satisfactorily. The major discrepancy remains the upward displacement of the modeled layer with respect to the observations during summer. In the model, the higher summertime Na layer is caused by changes in atomic O and $H_2O$. During summer, the general mesospheric circulation is characterized by an upwelling [e.g., *Garcia and Solomon*, 1985] which transports significant quantities of $H_2O$ to altitudes above 80 km, as shown in Figure 2. The vertical eddy diffusion between 80 and 100 km is also a maximum at this time of the year, so that atomic O is rapidly transported downward from above 100 km to the mesospheric sink region below 80 km, minimizing the O density below 100 km [*Garcia and Solomon*, 1985]. The resulting increase in $H_2O$ and decrease in O converts a higher proportion of Na to $NaHCO_3$ in the region between 80 and 90 km. Furthermore, inspection of Figure 1 shows that atomic O plays a significant role above 90 km in preventing $Na^+$ ions from forming clusters such as $Na.CO_2^+$ which can be neutralized by dissociative recombination with electrons [*Cox and Plane*, 1998]. Hence a decrease in atomic O between 90 and 100 km causes atomic Na to increase relative to $Na^+$. The overall result of both these effects is to cause an upward displacement of the layer during summer.

In fact, the discrepancy with the observations in summer is rather surprising. Lidar observations have shown that the

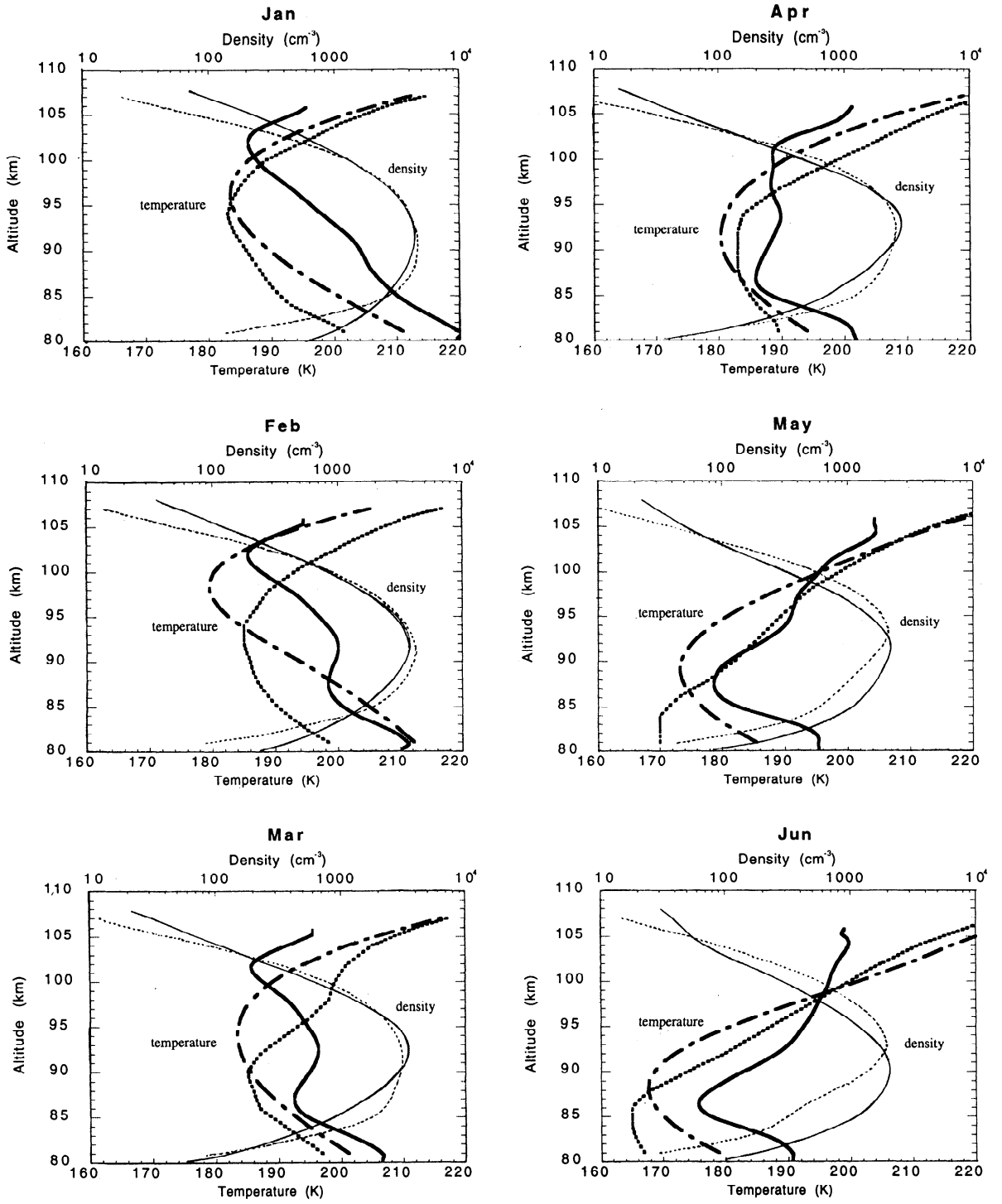


**Figure 4.** Measured (thin solid curves) and modeled (thin dotted curves) mean Na density profiles during each month at 40°N. Also shown are the measured temperature profiles (thick solid curves) which are compared with the Garcia-Solomon (thick dotted curves) and MSIS-E-90 (thick dash-dotted curves) models.

summertime Na layer at high northern and southern latitudes is displaced upward [*Gardner et al.*, 1988; *Kurzawa and von Zahn*, 1990; *Plane et al.*, 1998], in agreement with model predictions [*Helmer and Plane*, 1993; *Plane et al.*, 1998]. Furthermore, the excellent agreement shown in Figure 2 between $H_2O$ measured by UARS and predicted by the G-S model implies that the transport scheme within the G-S model is broadly correct. One factor contributing to the discrepancy in the present study could be the effect of tides on the lidar observations. During summer, the observation times are considerably shorter than in winter (vide supra), so that summer nighttime data sets are more susceptible to biases associated with incomplete sampling of both diurnal and semidiurnal tides. Recent papers by *Yu et al.* [1997] and *States and Gardner* [1998], and a current study at both

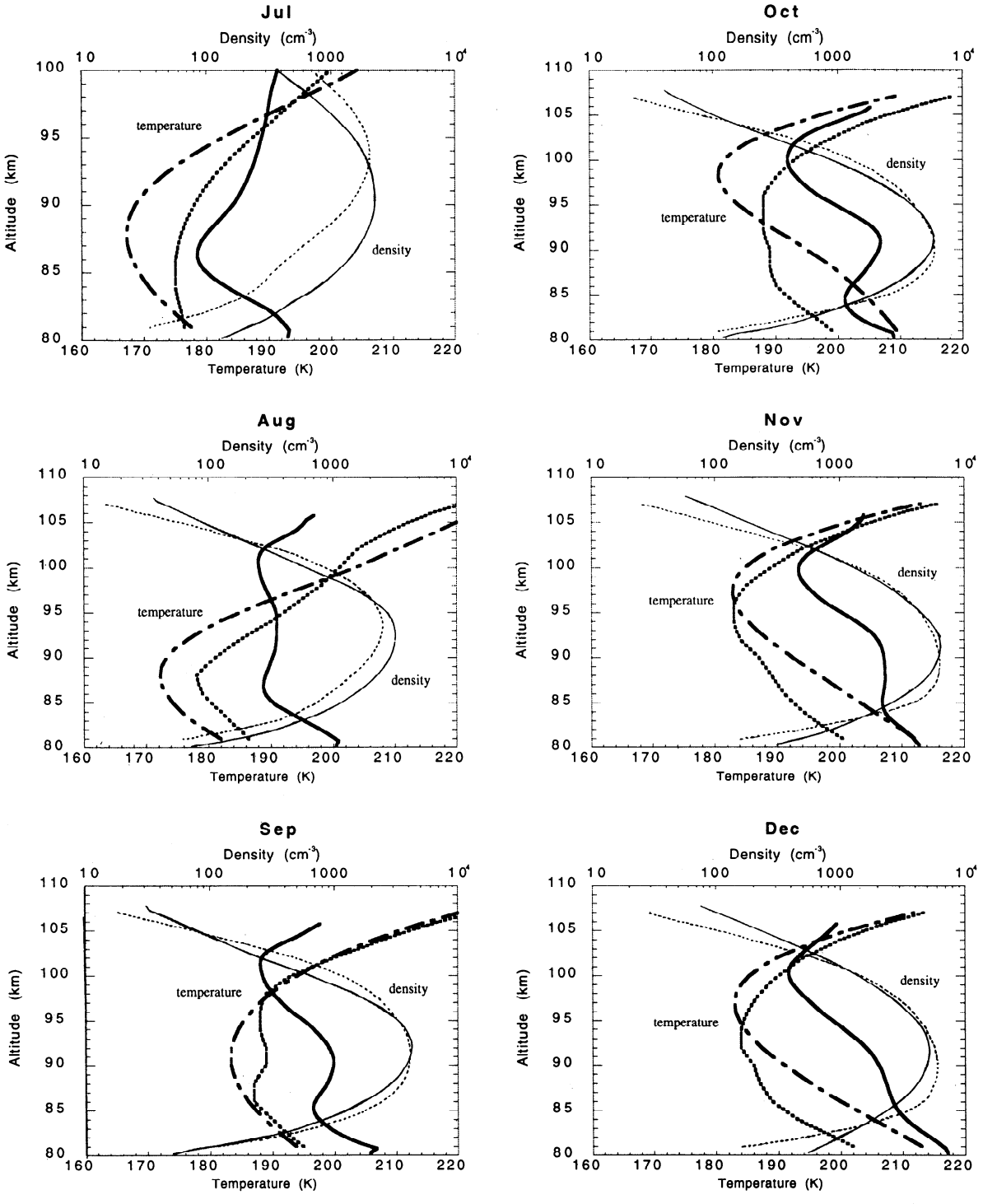


**Figure 4.** (continued)

Illinois and Colorado State where the summertime Na layer is being observed over a full diurnal cycle, should help to address this issue.

The observed annual mean Na density profile is plotted in Figure 5, and is well approximated by a Gaussian distribution with a centroid height of 91.6 km, rms width of 4.5 km, and abundance of 4.4 x $10^9$ $cm^{-2}$. Because the three adjustable parameters in the model were optimized to this annual mean profile, the modeled annual profile agrees very well as shown in Figure 5, with a centroid height of 91.7 km, rms width of 4.6 km, and abundance of 4.7 x $10^9$ $cm^{-2}$.

The column abundances, centroid heights, and rms widths of the nightly mean Na profiles are plotted against date in Figure 6. Because annual and semiannual variations are the strongest harmonic components of the seasonal fluctuations of these Na layer parameters, we have used minimum mean square error fits to determine the characteristics of these variations. The annual plus semiannual fits are plotted as thick curves in Figure 6, with the dashed curves lying one standard deviation above and below the fits. The amplitudes and phases of the fits are listed in Table 3. The Na column abundance variations are primarily annual with a maximum in winter, while both the centroid height and

**Table 2.** Gaussian Fits to the Monthly Mean Na Profiles

| | Jan. | Feb. | March | April | May | June | July | Aug. | Sept. | Oct. | Nov. | Dec. |
|---|---|---|---|---|---|---|---|---|---|---|---|---|
| Abundance $A_s$, $10^9$ cm$^{-2}$ | 6.20 | 4.52 | 3.63 | 2.92 | 2.55 | 2.32 | 2.64 | 3.72 | 4.51 | 6.19 | 7.53 | 6.63 |
| Centroid $z_o$, km | 91.4 | 91.7 | 92.3 | 92.4 | 91.0 | 90.4 | 90.9 | 92.0 | 91.8 | 91.3 | 91.4 | 91.7 |
| RMS width $\sigma_s$, km | 5.38 | 4.75 | 4.16 | 4.17 | 4.62 | 4.41 | 4.56 | 4.55 | 4.22 | 4.21 | 4.58 | 5.00 |

$$[\mathrm{Na}]_z = \frac{A_s}{\sqrt{2\pi}\sigma_s}\exp\left[\frac{-(z-z_o)^2}{2\sigma_s^2}\right]$$

rms width variations are primarily semiannual but about 180° (i.e., 90 days) out of phase. Notice that the night-to-night variability of all three parameters is quite large. In fact, the rms residuals from fitting the centroid height and rms width are comparable to the annual and semiannual amplitudes.

The modeled layer parameters are also plotted in Figure 6, demonstrating very good agreement for the column abundance: even though there is a small discrepancy between the model and the annual plus semiannual fit to the observations for October, November, and December, the model is actually in excellent agreement with the monthly average column abundances observed during these months. The modeled annual variation of the rms width is very nearly within one standard deviation of the fit to the observations throughout the year. However, the modeled centroid height is more than two standard deviations above the fit to the observations during summer. Note that the observed semiannual variation in the layer centroid height appears to be consistent with seasonal variations in the vertical eddy diffusivity [*Garcia and Solomon*, 1985]. That is, $K_E$ is large in summer and winter, and small at the equinoxes. Because of the close coupling between Na and O on the underside of the Na layer, further work is probably required here to understand in detail the interplay between the chemistry and dynamics of these species, which are both characterized by large mixing ratio gradients at these altitudes.

### 5.2. Seasonal Variations in Mesopause Region Temperatures

Figure 4 shows a comparison between the monthly temperature profiles measured by the Na lidars, and predicted by the G-S and MSIS-E-90 models. Plate 1c is a contour plot of the observed annual temperature variation as a function of altitude. The high winter mesopause is clearly evident in this plot and in the November, December, and January profiles in Figure 4. Likewise, the low summer mesopause appears in the May, June, and July profiles. By contrast, during the equinox periods of February though April and August through October, the profiles exhibit local temperature minima near the altitudes of both the summer and winter mesopauses. During these equinox transition periods the temperature profiles were observed to oscillate randomly between the nominal winter and summer states before stabilizing in May and November. Not surprisingly, the mean annual temperature profile (Figure 5) is a composite of the nominal wintertime profile with a high mesopause near 101 km, and the summertime profile exhibiting a low mesopause near 86 km.

The thermal structure of the global mesopause has been described by *She and von Zahn* [1998], based on a shipborne lidar observations made in 1996 between 71° S and 54° N [*von Zahn et al.*, 1996], and measurements at 41° N and 54° N during 1996-1997. The mesopause is observed to occur at two distinct altitudes: near 85 km in the summer hemisphere and near 100 km in the winter hemisphere, the transition from the summer altitude to the winter altitude occurring abruptly at about 30° in the summer hemisphere. Several discrepancies exist between these observations and current models, as depicted in Figure 4. First, the modeled mesopause altitude varies more smoothly between the winter and summer levels, and the observed altitude in winter is somewhat higher than the modeled value. Second, at midlatitudes, the observed monthly temperature profiles often show double temperature minima in spring and autumn, while modeled profiles exhibit this behavior only occasionally (see the September profile for the G-S model in Figure 4, and *She et al.* [1995, Figure 2]). But note that, since the difference between winter and summer mesopause temperatures is only 5-10 K at 40° N, wave perturbations and incomplete sampling of the diurnal and semidiurnal tides may be responsible for the frequent occurrence of nightly mean profiles with double temperature minima near the equinoxes. Third, depending on altitude, the modeled temperatures are lower than the observations shown in Figure 4 by some 20 K for MSIS-90, and 15 K for the G-S model. However, this discrepancy may be partly due to the fact that the lidar data in Figure 4 were taken between January 1991 and April 1994, during a period when the mesopause appears to have been warmer than usual (by as much as ~10 K in 1993), attributable to the Mount Pinatubo eruption [*She et al.*, 1998]. The G-S model calculations assume intermediate conditions between solar maximum and minimum, which is appropriate for the periods where the present data were taken.

The nightly mean mesopause temperatures and altitudes are plotted against date in Figure 7. The mesopause altitude was defined as the height of the coldest temperature in each nightly mean temperature profile. The solid curves are fits to the data including annual and semiannual variations, while the dashed curves are one standard deviation above and below the harmonic fits. The amplitudes and phases of the fits are listed in Table 3. The harmonic fits to both the mesopause temperature and altitude have strong annual components, varying from about 186 K at 100 km in mid-winter to about 170 K at 86 km in midsummer. These results are consistent with previously published analyses of subsets of this data [*Senft et al.*, 1994; *She et al.*, 1995; *Yu and She*, 1995]. Note that there is considerable night-to-night variability in the mesopause altitude and temperature caused by gravity waves, planetary waves, and tides. Although the rms residuals are larger than the amplitudes of the harmonic fits, the annual variation is clearly evident in the raw data plotted in Figure 7.

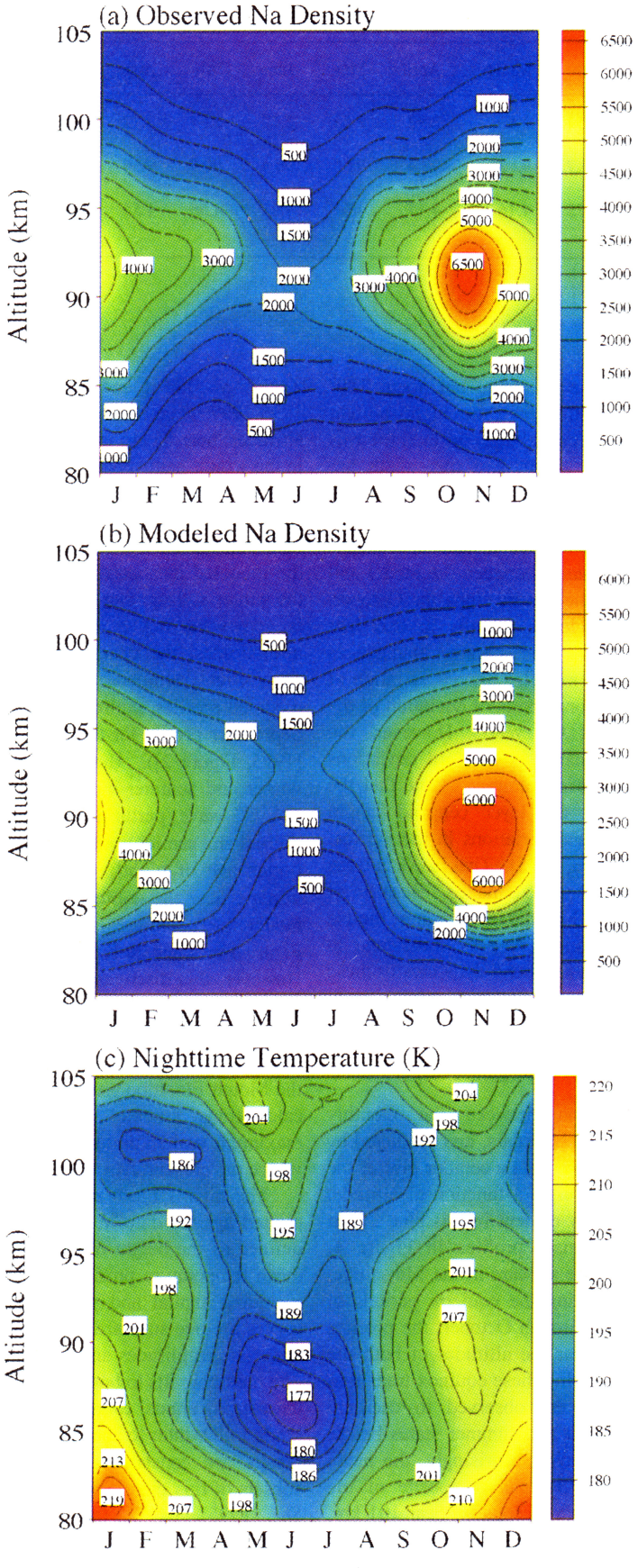


**Plate 1.** Contour plots of (a) measured Na density, (b) modeled Na density, and (c) measured temperature versus altitude and time. The measured data were generated by smoothing the nightly mean profiles using Hamming windows with full widths of 2 km and 45 days.

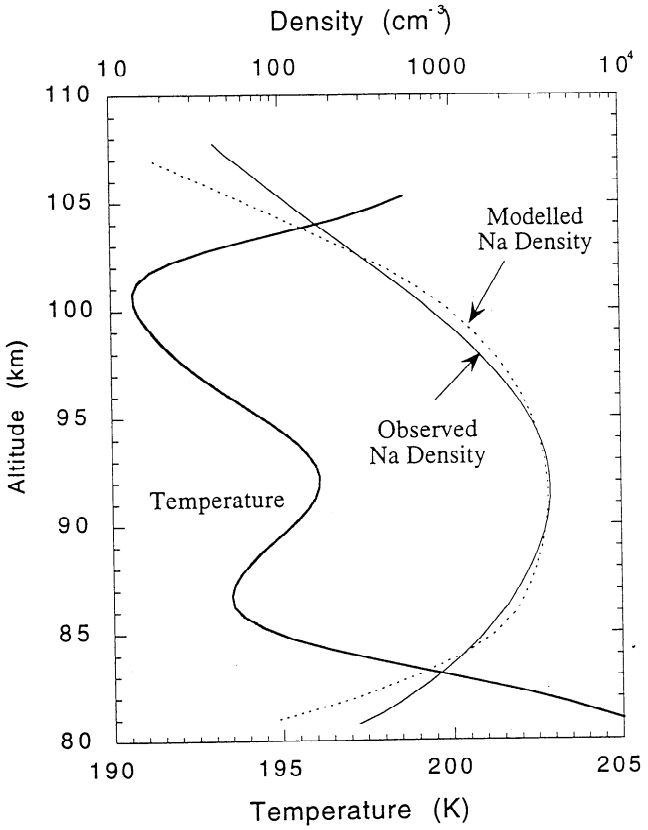


**Figure 5.** Annual mean profiles of the measured Na density (thin solid curve) and temperature (thick solid curve). The modeled mean Na density profile (thin dotted curve) is shown for comparison.

### 5.3. Comparison of Variations in Na Density and Temperature

In order to explore the relationships between Na density and temperature, we begin by determining the annual and semiannual components of their variations, as a function of altitude. The amplitudes and phases of the observed annual and semiannual variations in Na density are plotted in Figure 8. Annual variations dominate the Na perturbations at all altitudes over the layer, with an average amplitude of about 65%. The analogous plots for temperature in Figure 9 shows that annual variations dominate the temperature perturbations below 95 km, reaching a maximum amplitude of about 16 K at 86 km, while semiannual variations dominate above 95 km.

The seasonal variations in Na density and temperature therefore appear to be well correlated below about 95 km. This is confirmed by the profile of the Na-T correlation coefficient, plotted in Figure 10a. Below 96 km the correlation coefficient exceeds 0.7 at all altitudes reaching a maximum of 0.93 at 92 km, very near the annual mean centroid height of the Na layer. Above 96 km the coefficient decreases rapidly with increasing altitude, stabilizing near –0.2 above 100 km. Also shown in Figure 10a is the correlation coefficient profile computed from the model, which agrees extremely well with the measured correlation coefficient over the entire altitude range of the layer.

The model shows that below 96 km the temperature dependence of the odd oxygen/hydrogen chemistry largely determines the seasonal variation in Na density. Inspection of the temperature-dependences of $k_{29}$ and $k_{30}$ (vide supra) shows that at lower temperatures (during summer) the ratios of $[O_3]/[H]$ and $[O_3]/[O]$ increase. This, combined with the summertime increase of $H_2O$ above 80 km (Figure 2), has the effect of partitioning sodium into $NaHCO_3$ rather than atomic Na (see Figure 1). This effect is then reinforced by a secondary contribution from the temperature-dependent reactions involving

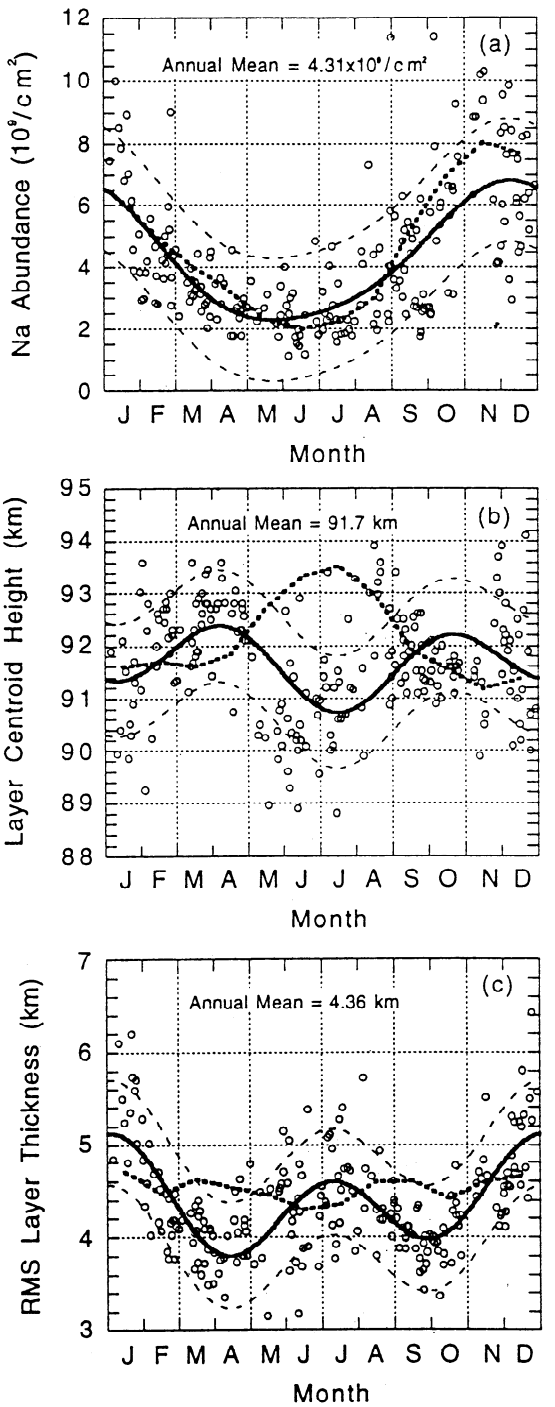


**Figure 6.** Plots of the Na layer (a) column abundance, (b) centroid height, and (c) rms width versus date. The data were computed from the nightly mean Na density profiles. The thick solid curves are least squares fits to the data including annual plus semiannual variations. The dashed curves are one standard deviation above and below the fits. The model predictions of these layer properties are shown as thick dotted curves.

**Table 3.** Annual Plus Semiannual Fits to the Mesopause Parameters

| Quantity | Mean $A_0$ | Annual Amplitude $A_1$ | Semiannual Amplitude $A_2$ | Annual Phase $d_1$, day | Semiannual Phase $d_2$, day | RMS Residual |
|---|---|---|---|---|---|---|
| Na layer abundance, $10^9$ cm$^{-2}$ | 4.26 | 2.24 | 0.33 | 338 | 167 | 1.70 |
| Na layer centroid height, km | 91.6 | 0.32 | 0.62 | 29 | 105 | 0.94 |
| Na layer RMS width, km | 4.38 | 0.28 | 0.47 | 353 | 6 | 0.42 |
| Mesopause temperature, K | 179.1 | 7.88 | 2.51 | 341 | 93 | 8.56 |
| Mesopause altitude, km | 94.78 | 5.74 | 2.11 | 350 | 57 | 5.50 |

$$x = A_0 + A_1 \cos\left[\frac{2\pi}{365}(d - d_1)\right] + A_2 \cos\left[\frac{4\pi}{365}(d - d_2)\right]$$

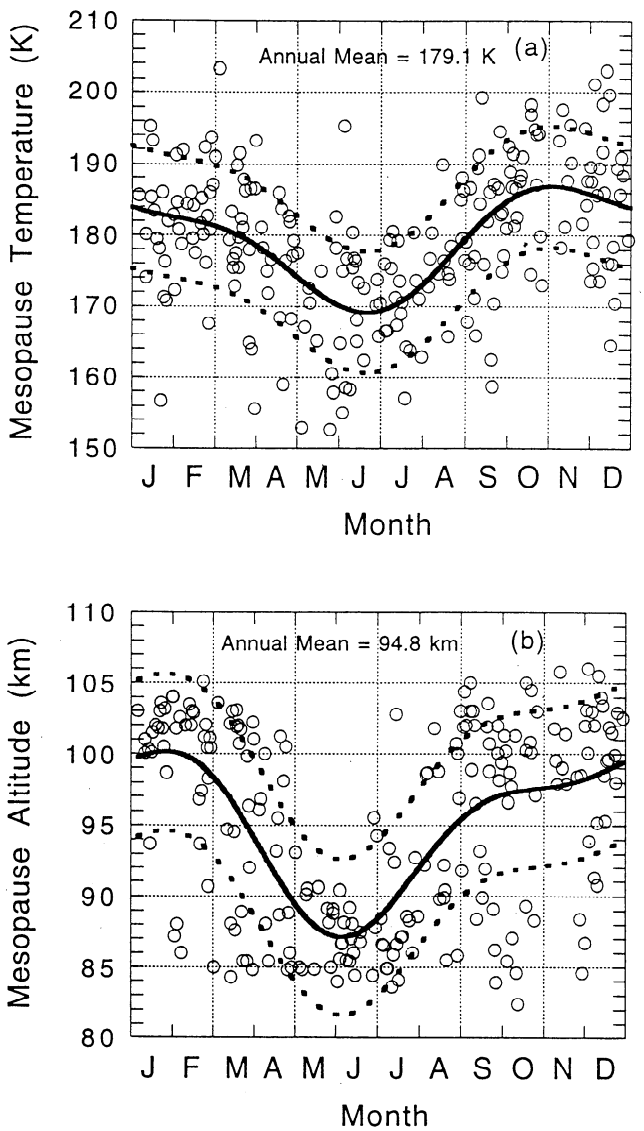


**Figure 7.** Plots of the mesopause (a) temperature and (b) altitude versus date. The data were computed from the nightly mean temperature profiles. The thick curves are least squares fits to the data including annual plus semiannual variations. The dashed curves are one standard deviation above and below the fits.

Na species themselves. As shown in Table 1, the reactions that oxidize Na to compounds such as $NaO_2$ and $NaHCO_3$ tend to be fast bimolecular processes with small activation energies, or recombination reactions with negative temperature dependences. By contrast, the reactions that convert these compounds back to atomic Na tend to be relatively highly activated. The overall effect is to produce the marked correlation between Na and T in Figure 10a.

Above 96 km, ion-molecule chemistry starts to dominate, and Na and $T$ become weakly anticorrelating because the rate of conversion of $Na^+$ to Na is controlled by two temperature-dependent factors. First is reaction (20) which forms the cluster $Na.N_2^+$; this is a recombination reaction with a negative temperature dependence. Second is reaction (22), the switching reaction between atomic O and $Na.N_2^+$ that prevents neutralization of the cluster (Figure 1). The rate of (R22) becomes slower at lower temperatures because of the decrease in atomic O (vide supra). Hence, both factors cause the rate of production of Na from $Na^+$ to increase at lower temperatures, contributing to the observed anticorrelation between Na and $T$.

Finally, the ratio of the rms Na density perturbation to the rms temperature perturbation is plotted against altitude in Figure 10b. Once again, there is good agreement between observation and model: the observed ratio peaks at a value of 315 cm$^{-3}$ K$^{-1}$ at 97 km, compared with a model prediction of 270 cm$^{-3}$ K$^{-1}$ at 96 km. Note that the peak of this ratio is about 5 km above the peak altitude of the Na layer. The reason for this is that although the rms Na density perturbation reaches a maximum at about 91 km, the rms temperature perturbation reaches a minimum only at about 97 km, in between the summer and winter mesopause heights.

### 5.4. Model Uncertainties

The sodium model presented here comprises two components: meteoric ablation with vertical transport, and gas-phase metal chemistry. However, these components are essentially decoupled because the gas-phase chemistry operates rapidly compared with vertical transport [*Plane et al.*, 1998], and so the uncertainties of each component can be considered separately. Beginning with the chemistry, much of the uncertainty has been removed by recent progress with laboratory studies of the pertinent elementary reactions. As shown in Table 1, the rate coefficients of most of the reactions in the model

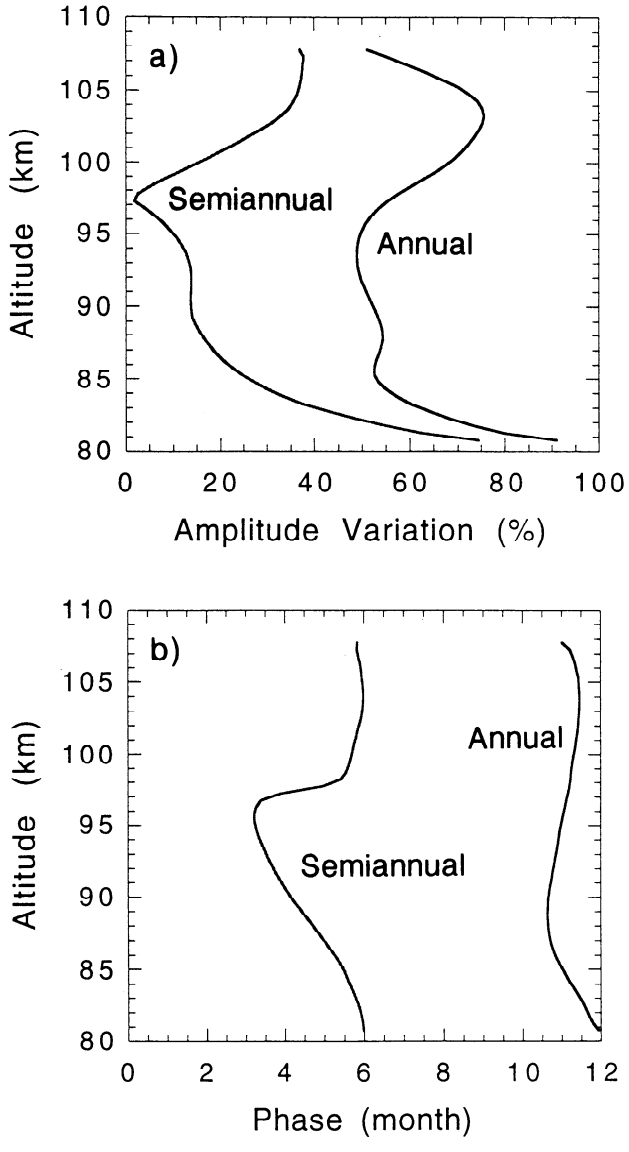


**Figure 8.** Profiles of the annual and semiannual (a) amplitudes and (b) phases of the seasonal Na density variations.

scheme have now been measured under appropriate conditions. Since the range of potential reactants in this region of the atmosphere is limited, it is unlikely that there are other major reservoir species besides $NaHCO_3$ and $Na^+$. Hence, although there are errors associated with individual rate coefficients, and $k_{17}$ in particular remains to be measured (although a current laboratory study at the University of East Anglia (UEA) indicates that the Arrhenius expression derived here is of the correct magnitude), the basic structure of the chemical scheme is unlikely to alter in the future.

Much greater uncertainty resides in the model component describing meteoric ablation, vertical transport, and the permanent sinks for the Na-containing species. Concerning ablation, the model is obviously sensitive to the total ablation flux of the Na species. The global influx of meteoric material is probably somewhat higher than the often quoted estimate by *Hughes* [1978]of 44 tons per day: for example, *Love and Brownlee* [1993] have recently derived a global influx of 110 tons per day from an experiment on the Long Duration Exposure Facility satellite. However, ablation models such as *Hunten et al.* [1980] predict that a significant fraction of this material will not vaporize. Hence the annual mean ablation flux of Na used here, $\Phi(Na) = 1.3 \times 10^4$ cm$^{-2}$ s$^{-1}$, is probably close to a lower limit, and the flux could be up to a factor of 2.5 larger. Note that the model is not particularly sensitive to the peak height of the ablation input: if this is changed in the model from 84.5 km [*Hunten et al.*, 1980] to 95 km as indicated from new radar measurements [*Elford et al.*, 1995], the predicted centroid height of the annual mean layer only changes from 91.7 to 92.4 km because eddy diffusion distributes the material vertically.

The model is in fact rather sensitive to the profile of the eddy diffusion coefficient. As explained above, the monthly profiles are calculated from the summertime profile derived by *Danilov and Kalgin* [1992], multiplied by a monthly scaling factor from the G-S model. This yields values for $K_E$ ranging from 1.0 to 3.0 x $10^6$ cm$^2$ s$^{-1}$ between winter and summer at 85 km. These are somewhat higher than the mean value of 6 x $10^5$ cm$^2$ s$^{-1}$ recommended by *Lübken et al.* [1993], based on in situ

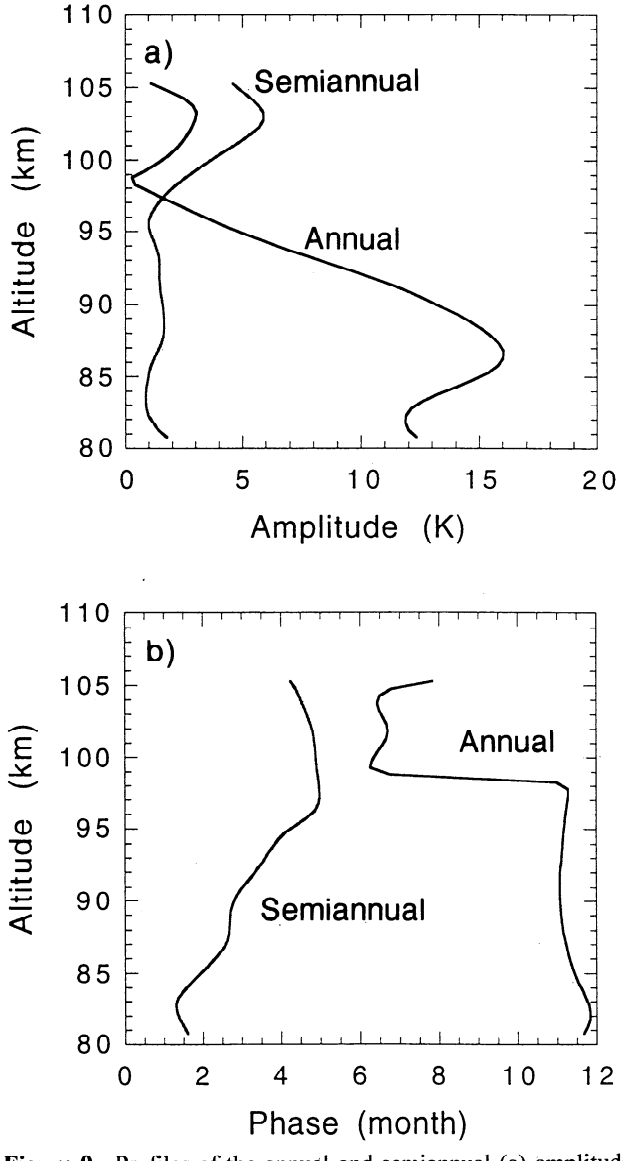


**Figure 9.** Profiles of the annual and semiannual (a) amplitudes and (b) phases of the seasonal temperature variations.

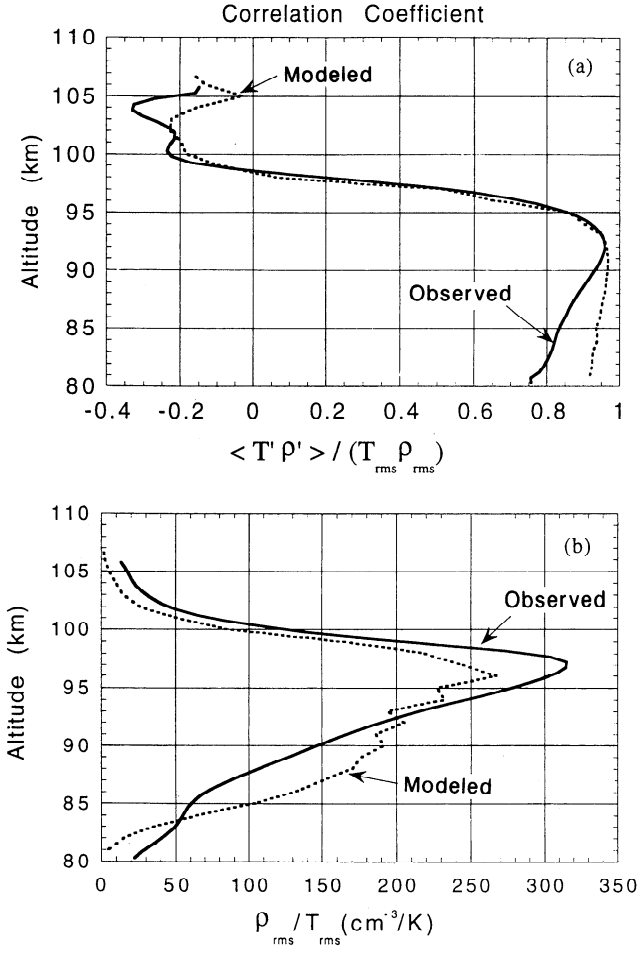


**Figure 10.** Measured and modeled profiles of (a) the correlation coefficient between the seasonal perturbations in Na density and temperature, and (b) the ratio of the rms seasonal Na density perturbations to the rms seasonal temperature perturbations.

measurements of small-scale density fluctuations. The G-S model (with $Pr$=5) predicts a mean $K_E$ at 85 km of only 2 x $10^5$ $cm^2$ $s^{-1}$. Indeed, when the G-S profiles for $K_E$ are used in the Na model, the concentration of total Na species builds up so that at 95 km (where most sodium is in the atomic form, see Figure 3), the concentration exceeds the observed Na density by a factor of at least 4. It is for this reason that we have used the larger $K_E$ profiles in the present model.

However, future work should explore this problem further. If $K_E$ is as small as predicted by the G-S model (and measured in some radar studies [e.g., *Fukao et al.*, 1994]), then a model will overpredict the Na layer unless the ablation flux is smaller (which is unlikely, *vide supra*), or the Na species are removed permanently in the mesosphere and are unable to cycle back to atomic Na. There are two obvious ways in which this can occur. As shown in Figure 3, $NaHCO_3$ is the major reservoir for sodium below 85 km. This molecule has a large dipole moment of 6.9 D [*Rajasekhar and Plane*, 1993], and so it is likely to polymerize easily and eventually form solid sodium bicarbonate, as was probably observed in a recent laboratory study [*Hildenbrand and Lau*, 1991]. It would also of course be expected to recombine with other metal-containing compounds. A second removal route is via heterogeneous loss on the surface of dust particles that have been proposed to form from the recondensation of meteoric debris [*Hunten et al.*, 1980]. Taking an estimated dust surface area of 1 x $10^{-9}$ $cm^2$ $cm^{-3}$ below 85 km [*Hunten et al.*, 1980], then an accommodation coefficient of 0.25 (i.e., 1 in every 4 collisions with the dust surface) or a lifetime against heterogeneous loss of about 8 days will remove Na species sufficiently quickly to reconcile a Na layer model with the smaller values of $K_E$. Finally, it should be noted that the total Na profile between 80 and 110 km, and hence the predicted atomic Na layer, is very similar irrespective of whether the larger $K_E$ profile is used with no permanent removal of $NaHCO_3$, as in the results presented here, or the smaller G-S values for $K_E$ are employed together with heterogeneous removal.

## 6. Conclusions and Summary

The first detailed picture of the seasonal variations of Na and temperature has been obtained from 3 years of lidar observations at two midlatitude sites. The Na density exhibits a strong annual variation at all heights between 81 and 107 km, with the column abundance peaking in early winter and then decreasing by nearly a factor of 4 to a midsummer minimum. There also appear to be significant semiannual components to the variations in the centroid height and rms thickness of the layer. The temperature profile between 81 and 105 km exhibits a high winter mesopause at about 101 km and a summer mesopause at about 85 km. During the spring and autumn equinox periods the mesopause oscillates apparently randomly between these states. A strong annual variation in temperature was observed between 81 and 96 km.

A detailed seasonal model of the Na layer was constructed from an established one-dimensional model by incorporating recent laboratory studies of the pertinent neutral and ionic chemistry of the metal. The background atmospheric composition was provided from three off-line models, as well as from UARS/MLS satellite measurements of $H_2O$. With a small number of permitted adjustable parameters, the model is able to reproduce many observed features of the Na layer remarkably well, including the monthly variation in column abundance and layer shape. The biggest discrepancy is during midsummer, when the modeled layer is displaced 2-3 km above that observed.

Both the observations and the model show that the Na density and temperature are highly correlated below 96 km, mostly as a result of the influence of odd oxygen/hydrogen chemistry on the partitioning of sodium between Na and the bicarbonate reservoir, $NaHCO_3$. Above 96 km a weak negative correlation is explained by the dominance of ion-molecule chemistry. The model also demonstrates that the small scale height on the underside of the Na layer is largely controlled by the falloff in atomic O. In the future it may be possible to exploit this relationship in order to estimate the falloff in O from lidar observations of Na.

Finally, it was found that if the eddy diffusion coefficient in the middle mesosphere is closer to $10^5$ $cm^2$ $s^{-1}$ as suggested by recent models and observations, rather than an order of magnitude higher, or if the global meteoric influx is over 100 tons per day, then models of the Na layer will have to include processes for permanently removing gas-phase Na species in the mesosphere, such as polymerization and deposition onto dust particles.

**Acknowledgments.** The modeling work at the University of East Anglia was supported by grant GST/02/1242 from the U.K. Natural Environment Research Council. The University of Illinois lidar work was supported in part by NSF grants ATM 94-03036 and ATM 97-09921 and by

NASA UARS grant NAG 5-2746. The work at Colorado State University was in part supported by NSF grants ATM 94-15853 and ATM 97-14676.

## References


Bilitza, D., K. Rawer, L. Bossy, and T. Gulyaeva, International Reference Ionosphere - Past, Present, Future, *Adv. Space Res.*, *13*(3), 3-23, 1993.

Bills, R. E., C. S. Gardner, and C. Y. She, Narrowband lidar technique for Na temperature and Doppler wind observations of the upper atmosphere, *Opt. Eng.*, *30*, 13-21, 1991a.

Bills, R. E., C. S. Gardner, and S. F. Franke, Na Doppler/Temperature lidar: Initial mesopause region observations and comparison with the Urbana MF radar, *J. Geophys. Res.*, *96*, 22701-22707, 1991b.

Bowman, M. R., A. J. Gibson, and M. W. C. Sanford, Atmospheric sodium measured by a tuned laser radar, *Nature*, *221*, 456-457, 1969.

Clemesha, B. R., D. M. Simonich, H. Takahashi, S. M. L. Melo, and J. M. C. Plane, Experimental evidence for photochemical control of the atmospheric sodium layer, *J. Geophys. Res.*, *100*, 18909-18916, 1995.

Collins, R., A. Nomura, and C. S. Gardner, Gravity waves in the upper mesosphere over Antarctica: Lidar observations at the South Pole and Syowa, *J. Geophys. Res.*, *99*, 5475-5485, 1994.

Committee on Space Programs and Research (COSPAR), International Reference Atmosphere: 1986, II, Middle atmosphere models, *Adv. Space Res.*, *10*(12), 1-519, 1990.

Cox, R. M., and J. M. C. Plane, An experimental and theoretical study of the clustering reaction between $Na^+$ ions and $N_2$, $O_2$ and $CO_2$, *J. Chem. Soc., Faraday Trans.*, *93*, 2619-2630, 1997.

Cox, R. M., and J. M. C. Plane, An ion-molecule mechanism for the formation of neutral sporadic Na layers, *J. Geophys. Res.*, *103*, 6349-6359, 1998.

Danilov, A. D., and U. A. Kalgin, Seasonal and latitudinal variations of eddy diffusion coefficient in the mesosphere and lower thermosphere, *J. Atmos. Terr. Phys.*, *54*, 1481-1489, 1992.

DeMore, W. B., S. P. Sander, D. M. Golden, R. F. Hampson, M. J. Kurylo, C. J. Howard, A. R. Ravishankara, C. E. Kolb, and M. J. Molina, Chemical kinetics and photochemical data for use in stratospheric modeling: Evaluation number 11, *JPL Publ. 94-26*, 1994.

Elford, W. G., M. A. Cervera, and D. I. Steel, Meteor velocities: A new look at an old problem, *Earth Moon Planets*, *68*, 257-266, 1995.

Fukao, S., M. D. Yamanaka, N. Ao, W. K. Hocking, T. Sato, M. Yamamoto, T. Nakamura, T. Tsuda, and S. Kato, Seasonal variability of vertical eddy diffusivity in the middle atmosphere, 1, Three-year observations by the middle and upper atmosphere radar, *J. Geophys. Res.*, *99*, 18973-18987, 1994.

Garcia, R. R., and S. Solomon, The effect of breaking waves on the dynamics and chemical composition of the mesosphere and lower thermosphere, *J. Geophys. Res.*, *90*, 3850-3868, 1985.

Garcia, R. R., and S. Solomon, A new numerical model of the middle atmosphere, 2, Ozone and related species, *J. Geophys. Res.*, *99*, 12937-12951, 1994.

Gardner, C. S., D. C. Senft, and K. H. Kwon, Lidar observations of substantial sodium depletion in the summertime Arctic mesosphere, *Nature*, *332*, 142-144, 1988.

Gibson, A., L. Thomas, and S. Bhattachacharyya, Lidar observations of the ground-state hyperfine structure of sodium and temperature in the upper atmosphere, *Nature*, *281*, 131-132, 1979.

Hedin, A. E., Extension of the MSIS thermospheric model into the middle and lower atmosphere, *J. Geophys. Res.*, *96*, 1159-1172, 1991.

Helmer, M., and J. M. C. Plane, "A study of the reaction $NaO_2 + O \rightarrow NaO + O_2$: Implications for the chemistry of sodium in the upper atmosphere, *J. Geophys. Res.*, *98*, 23207-23222, 1993.

Hildenbrand, D., and K. H. Lau, Mass spectrometric searches for gaseous sodium carbonates, *J. Phys. Chem.*, *95*, 8972-8975, 1991.

Hocking, W., Turbulence in the region 80-120 km, *Adv. Space Res.*, *10*(12), 153-161, 1990.

Hughes, D. W., Meteors, in *Cosmic Dust*, edited by J. A. M. McDonnell, pp. 123-185, John Wiley, New York, 1978.

Hunten, D. M., A meteor-ablation model of the sodium and potassium layers, *Geophys. Res. Lett.*, *8*, 369-372, 1981.

Hunten, D. M., R. P. Turco, and O. B. Toon, Smoke and dust particles of meteoric origin in the mesosphere and stratosphere, *J. Atmos. Sci.*, *37*, 1342-1357, 1980.

Jegou, J. P., C. Granier, M. L. Chanin, and G. Megie, General theory of the alkali metals present in the Earth's upper atmosphere, *Ann. Geophys.*, *3*, 163-176, 1985.

Juramy, P., M. L. Chanin, G. Megie, G. F. Toulinov, and Y. P. Doudoladov, Lidar sounding of the mesospheric sodium layer at high latitudes, *J. Atmos. Terr. Phys.*, *43*, 209-215, 1981.

Kane, T. J., and C. S. Gardner, Structure and seasonal variability of the nighttime mesospheric Fe layer at midlatitudes, *J. Geophys. Res.*, *98*, 16875-16886, 1993.

Kurzawa, H., and U. von Zahn, Sodium density and atmospheric temperature in the mesopause region in polar summer, *J. Atmos. Terr. Phys.*, *52*, 981-993, 1990.

Levandier, D. J., R. A. Dressler, S. Williams, and E. Murad, A high-temperature guided-ion beam study of $Na + X^+$ ($X = O_2$, NO, $N_2$) charge-transfer reaction, *J. Chem. Soc. Faraday Trans.*, *93*, 2611-2618, 1997.

Love, S. G., and D. E. Brownlee, A direct measurement of the terrestrial mass accretion rate of cosmic dust, *Science*, *262*, 550-553, 1993.

Lübken, F.-J., W. Hillert, G. Lehmacher, and U. von Zahn, Experiments revealing small impact of turbulence on the energy budget of the mesosphere and lower thermosphere, *J. Geophys. Res.*, *98*, 20369-20384, 1993.

McNeil, W. J., E. Murad, and S. T. Lai, Comprehensive model for the atmospheric sodium layer, *J. Geophys. Res.*, *100*, 16847-16855, 1995.

Papen, G. C., W. M. Pfenninger, and D. M. Simonich, Sensitivity analysis of sodium narrowband wind-temperature lidar systems, *Appl. Opt.*, *34*, 480-498, 1995.

Plane, J. M. C., The chemistry of meteoric metals in the Earth's upper atmosphere, *Int. Rev. Phys. Chem.*, *10*, 55-106, 1991.

Plane, J. M. C., and M. Helmer, Laboratory studies of the chemistry of meteoric metals, in *Research in Chemical Kinetics*, vol. 2, edited by R. G. Compton and G. Hancock, 313-367, Elsevier, New York, 1994.

Plane, J. M. C., R. M. Cox, J. Qian, M. Pfenninger, G. C. Papen, C. S. Gardner, and P. J. Espy, The mesospheric Na layer at extreme high latitudes in summer, *J. Geophys. Res.*, *103*, 6381-6389, 1998.

Pumphrey, H. C., and R. S. Harwood, Water vapor and ozone in the mesosphere as measured by UARS MLS, *Geophys. Res. Lett.*, *24*, 1399-1402, 1997.

Rajasekhar, B., and J. M. C. Plane, An *ab initio* study of dissociative electron attachment to $NaHCO_3$ and $NaCO_3$, and the role of these reactions in the formation of sudden sodium layers, *Geophys. Res. Lett.*, *20*, 21-24, 1993.

Senft, D. C., G. C. Papen, C. S. Gardner, J. R. Yu, D. A. Krueger, and C. Y. She, Seasonal variations of the thermal structure of the mesopause region at Urbana, Illinois (40° N, 88° W), and Fort Collins, Colorado (41° N, 105° W), *Geophys. Res. Lett.*, *21*, 821-824, 1994.

She, C. Y., and U. von Zahn, The concept of two-level mesopause: Support through new lidar observation, *J. Geophys. Res.*, *103*, 5855-5863, 1998.

She, C. Y., R. E. Bills, H. Latifi, J. R. Yu, R. J. Alvarez II, and C. S. Gardner, Two-frequency lidar technique for mesospheric sodium temperature measurements, *Geophys. Res. Lett.*, *17*, 929-932, 1990.

She, C. Y., J. R. Yu, H. Latifi, and R. E. Bills, High spectral resolution fluorescence light detection and ranging for mesospheric temperature measurements, *Appl. Opt.*, *31*, 2095-2106, 1992.

She, C. Y., J. R. Yu, D. A. Krueger, R. Roble, P. Keckhut, A. Hauchecorne, and M. L. Chanin, Vertical structure of the midlatitude temperature from stratosphere to mesopause (30-105 km), *Geophys. Res. Lett.*, *22*, 377-380, 1995.

She, C. Y., S. W. Thiel, and D. A. Krueger, Observed episodic warming at 86 and 100 km between 1990 and 1997: Effects of Mount Pinatubo eruption, *Geophys. Res. Lett.*, *25*, 497-500, 1998.

States, R. J., and C. S. Gardner, Influence of the diurnal tide and thermospheric heat sources on the formation of mesospheric temperature inversion layers, *Geophys. Res. Lett.*, *25*, 1483-1486, 1998.

Swenson, G. R., J. Qian, J. M. C. Plane, P. J. Espy, M. J. Taylor, D. N. Turnbull, and R. P. Lowe, Dynamical and chemical aspects of the mesospheric Na "wall" event on October 9, 1993, during the ALOHA Campaign, *J. Geophys. Res.*, *103*, 6361-6380, 1998.

Thomas, G. E., Global change in the mesosphere-lower thermosphere region: Has it already arrived?, *J. Atmos. Terr. Phys.*, *58*, 1629-1656, 1996.

Thomas, R.J., Total mixing ratios, *Planet. Space Sci.*, *22*, 175-177, 1974.

Tilgner, C., and U. von Zahn, Average properties of the sodium density distribution as observed at 69° N latitude in winter, *J. Geophys. Res.*, *93*, 8439-8454, 1988.

von Zahn, U., J. Höeffner, V. Eska, and M. Alpers, The mesopause altitude: Only two distinctive levels worldwide?, *Geophys. Res. Lett.*, *23*, 3231-3234, 1996.

Yu, J. R., and C. Y. She, Climatology of a midlatitude mesopause region observed by a lidar at Fort Collins, Colorado (40.6° N, 105° W), *J. Geophys. Res.*, *100*, 7441-7452, 1995.

Yu, J. R., R. States, S. Franke, C. S. Gardner, and M Hagan, Observations of tidal temperature and wind perturbations in the mesopause region above Urbana, Illinois (40° N, 88° W), *Geophys. Res. Lett.*, *24*, 1207-1210, 1997.

R. R. Garcia, National Center for Atmospheric Research, Boulder, CO 80307. (e-mail: (rgarcia@garcia.acd.ucar.edu)

C. S. Gardner, Department of Electrical and Computer Engineering, University of Illinois at Urbana-Champaign, Urbana, IL 61801. (e-mail: cgardner@uiuc.edu)

J. M. C. Plane, School of Environmental Sciences, University of East Anglia, Norwich NR4 7TJ, England, U.K. (e-mail: j.plane@uea.ac.uk)

H. C. Pumphrey, Department of Meteorology, University of Edinburgh EH8 9YL, Edinburgh, Scotland, U.K. (e-mail: hcp@met.ed.ac.uk)

C. Y. She, Department of Physics, Colorado State University, Fort Collins, CO 80521. (e-mail: joeshe@lamar.colostate.edu)

J. Yu, NASA Langley Research Center, Hampton, VA 23681.

(Received June 2, 1998; revised August 19, 1998;
accepted September 17, 1998.)